PHOTONICS Research

Supercontinuum generation in silicon photonics platforms

Christian Lafforgue,[1,2] Miguel Montesinos-Ballester,[1] Thi-Thuy-Duong Dinh,[1] Xavier Le Roux,[1] Eric Cassan,[1] Delphine Marris-Morini,[1] Carlos Alonso-Ramos,[1] and Laurent Vivien[1,3]

[1]Centre de Nanosciences et de Nanotechnologies (C2N), CNRS, Université Paris-Saclay, 91120 Palaiseau, France
[2]e-mail: lafforgue43@gmail.com
[3]e-mail: laurent.vivien@c2n.upsaclay.fr

Received 28 October 2021; revised 14 January 2022; accepted 14 January 2022; posted 19 January 2022 (Doc. ID 445304); published 1 March 2022

Nonlinear optics has not stopped evolving, offering opportunities to develop novel functionalities in photonics. Supercontinuum generation, a nonlinear optical phenomenon responsible for extreme spectral broadening, attracts the interest of researchers due to its high potential in many applications, including sensing, imaging, or optical communications. In particular, with the emergence of silicon photonics, integrated supercontinuum sources in silicon platforms have seen tremendous progress during the past decades. This article aims at giving an overview of supercontinuum generation in three main silicon-compatible photonics platforms, namely, silicon, silicon germanium, and silicon nitride, as well as the essential theoretical elements to understand this fascinating phenomenon.

https://doi.org/10.1364/PRJ.445304

1. INTRODUCTION

Since the first demonstrations of frequency conversion through second-harmonic generation in the early 1960s [1], applications based on nonlinear optics have not stopped flourishing. In particular, the generation of new frequencies led to the development of novel technologies in a multitude of domains. Nonlinear interaction of light with matter is responsible for a myriad of effects resulting in frequency conversion. An important breakthrough was the conception of Kerr frequency comb sources. Such a system is based on the nonlinear interaction of light waves, resulting in the generation of spectral rays equally spaced in the frequency domain. In particular, frequency comb sources based on microresonators pumped by a continuous wave (CW) laser were rapidly developed and showed the possibility of generating broadband comb sources. More generally, nonlinear optical effects can be exploited in different ways, giving a number of possibilities to achieve frequency conversion and broadband spectrum generation. Among them lies supercontinuum generation (SCG), consisting in an important spectral broadening from a narrowband pulsed light source. This nonlinear phenomenon is strongly related to the dispersion of the medium in which light propagates. For that reason, it has gained a great deal of interest in photonic crystal fibers (PCFs). Indeed, the design of the microstructure of PCFs permits tailoring the confinement and the dispersion of the optical mode propagating inside the fiber, allowing one to study and exploit SCG. Researchers have then made strong efforts to unravel the complex physical mechanisms responsible for SCG, involving several nonlinear processes, soliton dynamics, and linear propagation properties [2–9]. The strong development of this technology led to the emergence of novel applications based on SCG [10], such as ultrashort pulse generation, broadband sources for optical coherence tomography (OCT), octave spanning frequency comb generation for precise frequency metrology or for optical communications, and spectroscopy. Nevertheless, it is of particular interest to integrate such technology in compact and cost-effective photonic circuits. By doing so, it is possible to include SCG with other components on a single chip and so to build complex integrated photonics systems with reduced footprint and cost. As a matter of fact, integrated waveguides are very well adapted for SCG, as they permit tight confinement of light, interesting for nonlinear efficiency, and they offer many degrees of freedom for dispersion engineering via the choice of materials, the geometry, and the dimensions of the waveguide. The choice of materials is critical, as it determines the working wavelength range, the efficiency of nonlinear effects, and the fabrication methods. In general, silicon (Si) technology is under the spotlight in the photonics industry, as it is based on the same fabrication process flows as that of complementary-metal-oxide-semiconductor (CMOS) electronics. Si photonics has seen a rapid evolution, now showing exceptional performance. Modulators [11], all types of passive optical components [12–14], as well as detectors [15], have already been

demonstrated using Si and/or Si-compatible materials. Therefore, there is now a trend to develop efficient nonlinear devices using materials compatible with Si technology. This review article aims at giving an overview of SCG in Si photonics platforms. A high number of materials have been investigated, but for the sake of conciseness, this article is focused on three main Si compatible platforms, which are Si, silicon nitride (SiN_x), and silicon germanium (SiGe). This list is not exhaustive, but it gives a good and broad summary of the evolution of SCG in Si photonics. This review paper is organized in three main parts: first, a brief description of the main applications of SCG is given, followed by the theory behind this phenomenon, and finally, a state-of-the-art of SCG in Si photonics platforms is presented.

2. APPLICATIONS OF SCG

Many applications can benefit from the impressive features of SCG.

Spectroscopy:

First, in a quite simple way, SCG can be used as a broadband light source for absorption spectroscopy. In this case, the spectrum does not need to be coherent, as the method is only based on absorption phenomena in the tested samples, and the bandwidth of the supercontinuum determines the range of chemical species that can be identified: the broader the spectrum, the more species tested. By integrating an SCG source, it is possible to build a "lab-on-a-chip." The SCG source generates a broadband spectrum, an analyte can be deposited on a dedicated part on the chip, and a spectrometer can be used to obtain the absorbance spectrum, all on the same chip, for example. Also, more advanced techniques can be employed, such as dual comb spectroscopy, which this time requires the SCG source to be coherent.

Imaging:

SCG is also found useful for imaging techniques that require broadband light sources, such as confocal microscopy [16] or OCT [5,17,18]. To give an example, in the case of time-domain OCT, the bandwidth of the pulsed light source determines the performance of the imaging techniques: a broader spectrum means a faster, more sensitive and higher resolution imaging technique. For better performance, it is also desirable to work with coherent spectra (so with low-intensity noise due to pulse-to-pulse fluctuations) for OCT to minimize the integration time needed to perform an acquisition [19,20].

Optical communications:

The rapid evolution of demand in communication leads to new technological requirements. The use of optical communication answers several bottlenecks thanks to wavelength division multiplexing schemes. Such a method requires many optical carriers. These carriers can be obtained by using several CW laser sources (one for each carrier), or in a more cost-effective and practical way, with a frequency comb source [7,21–24]. SCG is an efficient way to generate broadband frequency combs: a high repetition rate pulsed laser source (from a mode-locked laser for example) can be used to trigger SCG in a waveguide, creating a broad frequency comb with a free spectral range determined by the repetition rate of the source. SCG could be an interesting alternative for the use of dense wavelength division multiplexing in telecommunication systems.

Frequency metrology:

In the frame of the frequency comb, SCG covering more than one octave is of prime interest. Indeed, it permits one to stabilize the comb through the precise determination of the carrier envelope offset frequency by mean of f-to-$2f$ interferometry. Since this technique requires interfering between the supercontinuum spectra and its second harmonic, the spectrum must cover at least one octave and be coherent. A feedback loop can then be implemented to stabilize the frequency comb. This technique allows one to determine the position of the frequency comb teeth, achieving excellent precision for frequency metrology [25,26]. In particular, it is especially used in the field of optical clocks, as it gives extremely high resolution in frequency measurement [27].

3. THEORETICAL BACKGROUND

This section aims at giving the essential elements of the theory behind SCG. For deeper details, several articles and books give a complete theory of SCG and pulse propagation in nonlinear media [4,28,29]. Nevertheless, this part should give the reader enough information to understand the origin and conditions of SCG.

We consider an electric field $\mathbf{E}$ in the form of a short optical pulse,

$$\mathbf{E}(x,y,z,t) = \frac{1}{2}[A(z,t)\mathbf{F}(x,y)\exp(i\beta_0 z - i\omega_0 t) + \text{c.c.}]. \quad (1)$$

Here, x, y are the transverse coordinates, respectively, to the propagation axis z, $A(z,t)$ is the temporal envelope of the pulse, $\mathbf{F}(x,y)$ is the transverse modal distribution, and β_0 and ω_0 are the propagation constant and the angular frequency of the carrier wave, respectively. The abbreviation "c.c." stands for "complex conjugate."

Such a short pulse can reach very high peak intensity, which enables one to trigger strong nonlinear effects. Nonlinear optical phenomena then arise from the creation of a nonlinear dielectric polarization, which then modifies the way in which the optical pulse propagates.

A. Pulse Propagation in a Nonlinear Medium

Under the hypothesis of a slowly varying envelope, the propagation of an optical pulse in a material exhibiting third-order nonlinearity only (modeled by the third-order susceptibility tensor $\chi^{(3)}$) is ruled by the generalized nonlinear Schrödinger equation (GNLSE), describing the evolution of the pulse envelope during propagation [29],

$$\begin{aligned}&\frac{\partial A}{\partial z} + \frac{\alpha}{2}A - i\sum_{k\geq 2}\beta_k \frac{i^k}{k!}\frac{\partial^k A}{\partial T^k}\\ &= i\gamma\left(1 + i\tau_s\frac{\partial}{\partial T}\right)\left[(1-f_r)|A|^2 A\right.\\ &\left.\quad + f_r A\int_0^\infty h_r(T')|A(z,T-T')|^2 \mathrm{d}T'\right]. \quad (2)\end{aligned}$$

Here, α is the linear propagation loss coefficient, T represents a time frame moving alongside the pulse at the group velocity ($T = t - z/v_g$), and β_k are the dispersion coefficients

defined by the Taylor series of the propagation constant around the center frequency $\beta(\omega)$. It is of great importance to consider this frequency dependence of β, since we consider optical fields with broad spectra. The coefficient β_2 is called group velocity dispersion (GVD), a key parameter in pulse propagation, and $\beta_{k>2}$ are referred to as higher-order dispersion (HOD). On the right-hand side of Eq. (2), γ is the nonlinear coefficient defined as $\gamma = \omega_0 n_2/(cA_{\text{eff}})$, with n_2 being the nonlinear refractive index (proportional to $\chi^{(3)}$) and A_{eff} being the nonlinear effective mode area. The time constant τ_s models the frequency dependence of γ to the first order, and the integral term is related to the delayed nonlinear response due to the Raman effect, modeled by its temporal response $h_r(t)$ and its fractional contribution f_r. Here, the terms corresponding to multiphoton absorption are omitted for clarity, but they can be added depending on the type of nonlinear absorption. In the case of multiphoton absorption, an additional term of linear loss can also be added to model the associated free-carrier absorption.

To better understand the different regimes of pulse propagation, it is interesting to first focus on the contributions of self-phase modulation (SPM) (related to γ) and GVD (related to β_2).

1. SPM

The main nonlinear effect contributing to SCG is SPM. It is based on the intensity-dependent refractive index of the nonlinear material n [29],

$$n = n_0 + n_2 I, \tag{3}$$

where n_0 is the linear refractive index, I is the optical intensity, and n_2 is the nonlinear index ($n_2 > 0$ in most of the cases), related to $\chi^{(3)}$. This causes the optical wave to acquire an intensity-dependent phase: at higher intensity, the refractive index is higher, meaning that the carrier wave travels more slowly, while it travels faster in the tails of the envelope, as depicted in Fig. 1. In the frequency domain, sidelobes appear within the spectrum around the center frequency, while accumulating a frequency-dependent phase during propagation. Qualitatively, it can be interpreted as the appearance of fast lower-frequency components and slow higher-frequency components. The importance of SPM during propagation is commonly characterized by the so-called nonlinear length $L_{\text{nl}} = 1/(\gamma P_0)$ [29], with P_0 being the peak power of the optical pulse. L_{nl} corresponds to the length at which the center of the pulse accumulates a phase shift of 1 rad.

2. GVD

By definition, GVD is responsible for a frequency-dependent group velocity. More practically, it means that at a given distance, each frequency component of the initial pulse has a different delay, or phase, with respect to the center frequency. In the temporal domain, the pulse duration increases, while the peak intensity decreases during propagation. Note that in the literature, GVD is also often described by the dispersion parameter defined by $D = -\omega_0^2 \beta_2/(2\pi c)$. Based on the sign of the GVD, two different regimes are possible, as shown in Fig. 1(b):

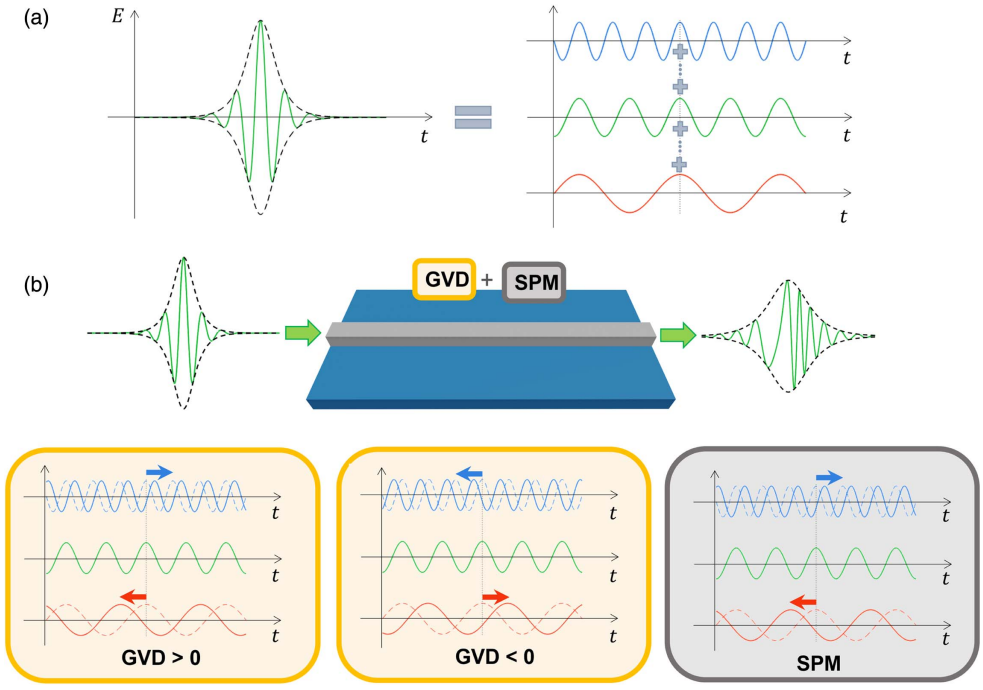

Fig. 1. Schematic representation of the effect of SPM and GVD on an optical pulse. (a) Simplified representation of an optical pulse with the carrier wave (green curve) shaped by a temporal envelope (black dashed curve). The pulse is the summation of several frequency components. Three of these components are schematically represented on the right graph (high-frequency in blue, central-frequency in green, and low-frequency in red). (b) Simplified representation of the processes of SPM and GVD along a waveguide. Both effects play a role on the relative phase of each spectral component of the initial pulse: each spectral component of the pulse is delayed or advanced relative to the carrier wave (green curve) after propagating in the waveguide.

• a normal dispersion regime when $\beta_2 > 0$ ($D < 0$), meaning that higher-frequency components travel more slowly than lower-frequency ones;
• an anomalous dispersion regime when $\beta_2 < 0$ ($D > 0$), meaning that higher-frequency components travel faster than lower-frequency ones.

Similarly, as for SPM, a characteristic length is defined for the GVD, $L_d = T_0^2/|\beta_2|$, with T_0 being the pulse duration [29]. It corresponds to the distance at which a Gaussian optical pulse undergoes a temporal broadening of a factor $\sqrt{2}$.

It can be seen that in the normal dispersion regime, the evolution of the phase is of the same type as the one due to SPM, while in the anomalous dispersion regime, GVD and SPM have opposite consequences. These two cases naturally lead to different behaviors in the process of SCG. Furthermore, a singular feature of anomalous dispersion regime is the unstable nature of solutions of Eq. (2). Indeed, with $\beta_2 < 0$, a small perturbation of the initial conditions, typically due to noise, can be amplified through phase-matched four-wave mixing processes, leading to amplification of the perturbation during propagation. This phenomenon, known as modulation instability (MI), causes phase and intensity fluctuations, which in turn greatly affect the coherence of the supercontinuum spectrum.

Even if in many cases materials exhibit normal dispersion, GVD can be tailored by playing on the waveguide's geometry and compensate the normal material dispersion with the waveguide dispersion.

3. Coherence

In this article, the term coherence refers to the phase stability across the spectrum from one pulse to another. It is commonly described by the modulus of the first order of mutual coherence g_{12}, defined as follows [4,29]:

$$|g_{12}(\omega)| = \left| \frac{\langle \tilde{A}_1^*(\omega)\tilde{A}_2(\omega)\rangle}{\sqrt{\langle|\tilde{A}_1(\omega)|^2\rangle\langle|\tilde{A}_2(\omega)|^2\rangle}} \right|. \tag{4}$$

Here, $\tilde{A}_1(\omega)$ and $\tilde{A}_2(\omega)$ are the Fourier transform of the temporal envelopes $A_1(t)$ and $A_2(t)$ of two independent pulses. The angle brackets $\langle\cdot\rangle$ denote an ensemble average over a high number of pairs of independent spectra. $|g_{12}|$ close to 1 means a high coherence (high phase stability), while $|g_{12}|$ close to 0 means a poor coherence (unstable phase).

Using this definition, the coherence can be theoretically determined through a high number of simulations, and it can be measured using interferometric techniques [30].

B. Pumping Regimes

1. Normal Dispersion Regime

By pumping a waveguide in the normal dispersion regime, spectral broadening is obtained through basic SPM. In this case, the bandwidth is generally quite small, since uncompensated GVD gradually reduces the intensity and increases the duration of the optical pulse. Since SPM is proportional to the intensity, spectral broadening is limited by the effect of GVD. Nevertheless, this scenario has the great advantage of imparting a highly coherent spectrum, since it is not sensitive to noise because MI is absent. Propagation of a pulse in the normal dispersion regime is also known to create a linear frequency chirp, which is especially adequate for pulse compression [31,32]. Moreover, the combination of positive GVD and SPM gives rise to an intriguing behavior responsible for the generation of flat supercontinuum spectra [33]: in this situation, the highly frequency-shifted components from the center of the pulse due to SPM can overtake the nonshifted components located at the tails of the temporal pulse in the temporal domain. This phenomenon, called optical wave breaking (OWB), causes oscillations at the pulse edges due to the temporal overlap of two different frequency components interfering. The pulse acquires a flattop shape in the temporal domain. Additionally, it has been shown that when a pulse traveling on a distance long enough for OWB to occur, the spectrum becomes significantly flatter than in the case without OWB. The specific dynamics of pulse propagation in the normal dispersion regime is detailed in Fig. 2(a). In order to enhance OWB, waveguides can be designed in a way that the dispersion length L_d is reduced: the higher $|\beta_2|$, the lower L_d.

For these reasons, according to the conditions and the application, it can be of great interest to work in the normal dispersion regime, as it can offer flat and coherent broad spectra.

2. Anomalous Dispersion Regime

On the other hand, when pumped in the anomalous dispersion regime, GVD and SPM play opposite roles, meaning they can compensate for each other. This particular interplay between both effects is responsible for a particular type of optical pulses: solitons. Indeed, if GVD and SPM perfectly compensate for each other (when $L_d = L_{\mathrm{nl}}$), the initial optical pulse does not see any deformation during propagation. This distortionless wave is called a fundamental soliton. Also, GVD can periodically catch up SPM, resulting in a periodic behavior of the pulse with the propagation distance, corresponding to a higher-order soliton. Such a light pulse is characterized by the so-called soliton order (N), which depends on the GVD, the nonlinear parameter of the waveguide, the initial pulse duration T_0, and peak power P_0 [29],

$$N = \sqrt{\frac{L_d}{L_{\mathrm{nl}}}} = \sqrt{\frac{\gamma P_0 T_0^2}{|\beta_2|}}. \tag{5}$$

Without any HOD or other nonlinear effect than SPM, no SCG is obtained, since the pulse constantly alternates between low and high bandwidth, periodically recovering its original shape. However, such solutions are known to be sensitive to perturbations: a change in an nth order soliton condition breaks it into N fundamental solitons, covering a much higher bandwidth than the initial pulse. The peak powers P_j and the temporal widths T_j of these solitons can be predicted by the following formulas [34]:

$$P_j = P_0 \frac{(2N - 2j + 1)^2}{N^2}, \qquad T_j = \frac{T_0}{2N - 2j + 1}, \tag{6}$$

where $j = 1, \ldots, N$. The distance at which soliton fission occurs is difficult to theoretically evaluate, and several definitions can be found in the literature. For instance, Dudley *et al.* used $L_{\mathrm{fission}} \sim L_d/N$ to approximate the fission length [4]. Perturbations responsible for such soliton fission can be of multiple origins: HOD, self-steepening effect, or stimulated Raman scattering (SRS) are the most common causes of this

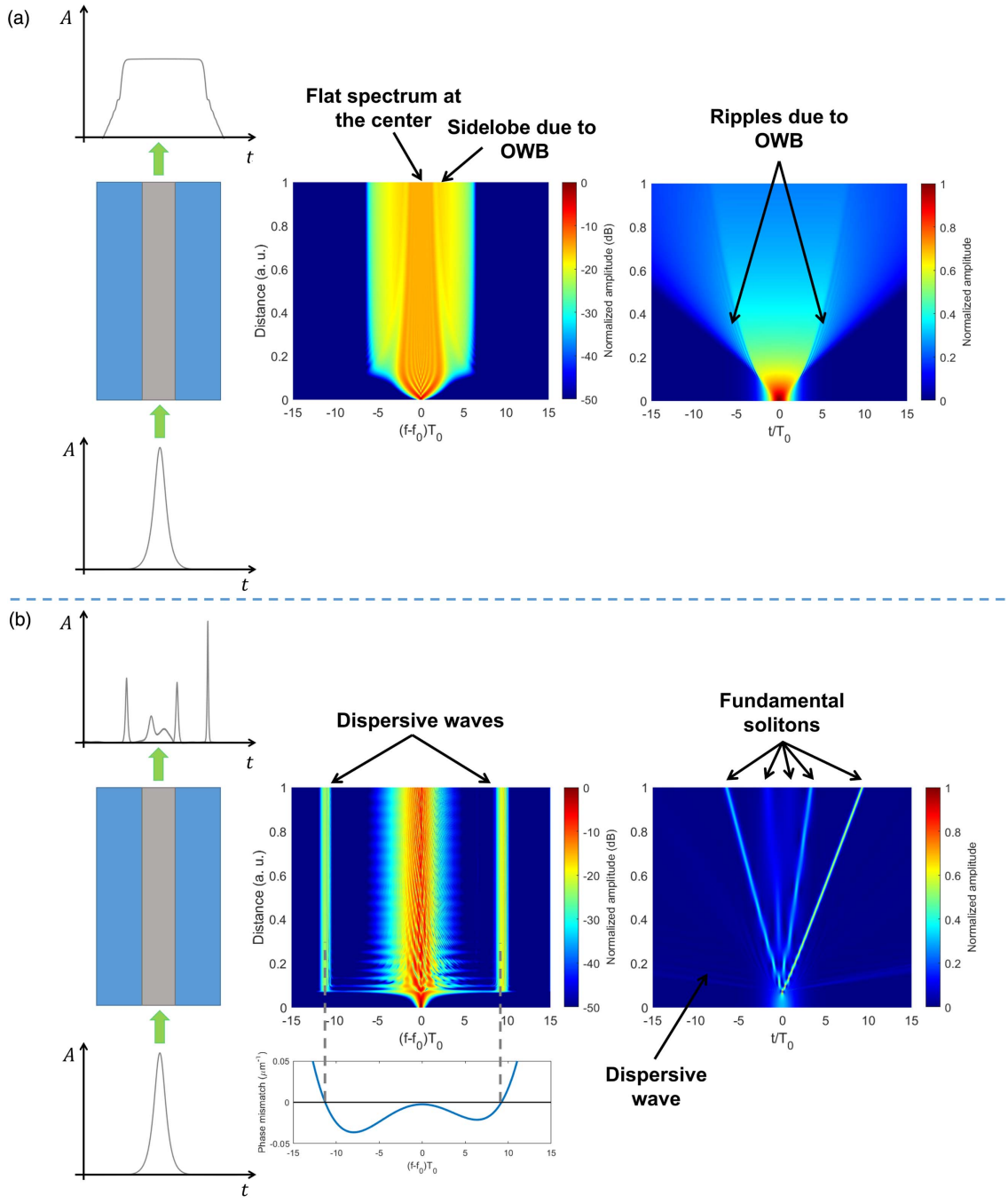

Fig. 2. Numerical simulation of a pulse propagating in a nonlinear medium. (a) Propagation in the normal dispersion regime, showing OWB; (b) SCG resulting from soliton fission of a fifth-order soliton in presence of third- and fourth-order HOD. The phase mismatch graph, calculated from Eq. (7), shows the prediction of the DW positions (zero-crossing points).

pulse breakup. Perturbation due to HOD presents an interesting feature: the optical pulse initially evolving in anomalous dispersion regime sees its spectrum overlapping with normal dispersion regions during its broadening. This configuration allows the existence of dispersive waves (DWs) in the normal dispersion regime that are phase-matched with the soliton in the anomalous dispersion regime. Figure 2(b) shows a simulation of the fission of a fifth-order soliton leading to SCG with the generation of two DWs due to third- and fourth-order HOD. The first soliton that is ejected during the fission has the highest peak power and the smallest duration (and so the highest bandwidth). For that reason, in general, DWs are mainly due to this soliton. Note that the frequency of DWs can be predicted by solving a nonlinear phase-matching equation [4],

$$\beta(\omega_{\mathrm{DW}}) - \beta(\omega_s) - \frac{\omega_{\mathrm{DW}} - \omega_s}{v_{g,s}} - \frac{\gamma P_s}{2} = 0, \tag{7}$$

where ω_{DW} and ω_s are the angular frequencies of the DWs and the first ejected soliton, respectively, and $v_{g,s}$ and P_s are the group velocity and the peak power of the latter. The center angular frequency ω_s of the soliton is not easy to know, but approximating it with ω_0 is generally sufficient. The peak power of the first ejected soliton can be deduced from the order of the initial soliton before fission using Eq. (6) with $j = 1$. In some cases, additional perturbation comes from SRS. This interaction of photons with vibrational modes of the nonlinear material continuously redshifts the soliton frequency and reduces the amount of power transferred to DWs. This phenomenon is predominant in optical fibers, but it is usually negligible in integrated waveguides.

Usually, SCG in anomalous dispersion is broader than in the normal dispersion case because of the particular soliton dynamics. However, MI can have a significant impact on the SCG process and spectra often feature important fluctuations. MI can even break the coherence of the spectrum, which can be troublesome, depending on the application. MI can be induced by SPM if the spectral width of the pulse reaches the maximum MI gain zones. For a Gaussian pulse, this happens at a distance $L_{mi,spm} = \sqrt{2L_d L_{nl}}$ [29]. Important perturbations can also come from noise (quantum shot noise or relative intensity noise of the source, for example), triggering spontaneous MI. Dudley *et al.* stated that noise amplified by MI significantly perturbs the pulse propagation after a distance $L_{mi,noise} \sim 16L_{nl}$ [4]. From this, it can be considered that the condition $N \ll 16$ is adequate for coherent SCG, ensuring $L_{fission} \ll L_{mi,noise}$.

It is noteworthy to highlight that SCG in the anomalous dispersion regime can also be obtained with a CW input by taking advantage of MI. MI can transform a CW pump into a train of short pulses, which can then trigger the SCG process [29]: a small perturbation of the CW pump (which can be induced by another CW source) with frequencies within the MI gain sidebands will get amplified during propagation and modulate the carrier CW wave into optical pulses.

To summarize, SCG results from a complex interplay between many physical effects, mainly based on third-order nonlinear effects and dispersion. Several ways exist to achieve SCG, either in the normal or in the anomalous dispersion regimes, with pulsed sources or CW sources. Each method presents different assets and drawbacks in terms of bandwidth, coherence, and integration. Therefore, the type of supercontinuum must be chosen according to the targeted application.

4. SCG IN Si-BASED DEVICES

Si is naturally the first choice one can think about for CMOS fabrication techniques compatibility. Moreover, Si possesses a very high nonlinear index ($n_{2,Si} \approx 6.3 \times 10^{-18}$ m^2/W), 2 orders of magnitude higher than that of SiO_2 (commonly used in nonlinear fiber optics) [35], as shown in Fig. 3, and a high refractive index ($n_{Si} \approx 3.48$ at a wavelength of 1.5 μm), which results in a high index contrast with the surrounding insulator ($n_{SiO_2} \approx 1.45$ at a wavelength of 1.5 μm). This important index contrast leads to a very tight confinement of light in the Si core, interesting to enhance nonlinear effects as the power density in the Si core can then be extremely high. In general, the nonlinear parameter γ in Si waveguides is within the order

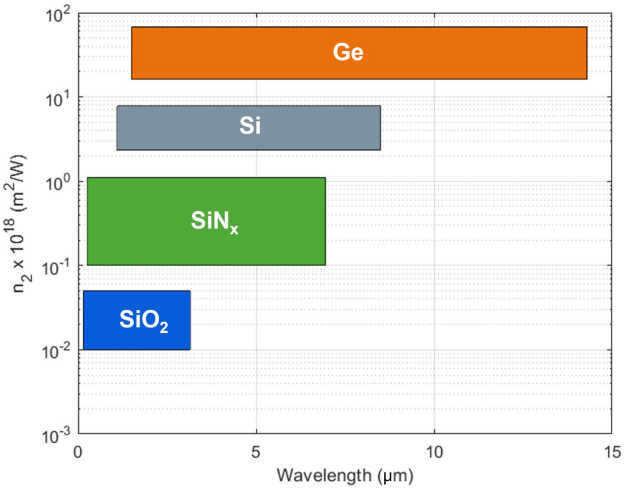

Fig. 3. Nonlinear index of commonly used materials in Si nonlinear photonics over their transparency windows. The height of the boxes represent the range of variation and the uncertainties on the values of n_2.

of 100 W^{-1} m^{-1}. The transparency window of Si extends from 1.1 to 8.5 μm, and thanks to the maturity of fabrication processes, linear propagation losses can be reduced to subdecibel per centimeter levels. However, taking into account two photon absorption (TPA), the lower bound of the transparency range is shifted to 2.2 μm [35], which strongly limits the use of Si for SCG when pumping in the classic optical communication bands. This limitation can be seen in the work of Hsieh *et al.*, who experimentally demonstrated for the first time continuum generation in the anomalous dispersion regime in 4.7 mm long Si waveguides in 2007 [36]. The tested waveguide has a cross section of 520 nm × 220 nm and was pumped by a pulsed source with a repetition rate of 250 kHz, a duration of 100 fs, and an average power of 1 W. Although the confinement and dispersion properties of the waveguide resulted in a highly effective nonlinear effect at $\lambda = 1.3$ μm, TPA limited the bandwidth of the spectrum to a 3/10 octave span. The important influence of TPA on the SCG bandwidth is also confirmed by the numerical work of Yin *et al.* [37]. For that reason, Si is generally used for SCG in the mid-infrared (mid-IR) region, interesting for spectroscopy applications, as a tremendous number of chemical compounds have absorption signatures in this domain. Mid-IR SCG is also interesting for imaging techniques like OCT, as the penetration depth in a 3D sample increases with the wavelength [17]. Still, some efforts have been made to achieve SCG in the near-IR range despite the effect of TPA.

A. Near-IR SCG Demonstrations in Si

The silicon on insulator (SOI) platform, composed of a patterned Si core on a buried oxide (BOX) layer made of SiO_2, is the most commonly used structure in Si photonics due to its high maturity and low cost. There is a high index contrast between both materials, and low linear loss can be achieved. However, the transparency window of SiO_2 stops at about 3.6 μm, hence limiting the range of wavelengths that can be used to pump the waveguide and to achieve spectral broadening. Still, great efforts were made to exploit the SOI platform

for SCG due to its high potential of integration. In the early stages of SCG development on the SOI platform, the SCG bandwidth was limited to less than an octave. In 2012, numerical studies showed the possibility to generate an octave-spanning supercontinuum using a dispersion-engineered SOI slot waveguide [38]. In this numerical work, the input optical pulse is arbitrary, taken to have a duration of 120 fs and a peak power of 62 W at a center wavelength of 1810 nm in the anomalous dispersion regime. The authors proposed a way to tailor the dispersion profile in order to create a flat, wide anomalous dispersion window (from 1418 to 2108 nm in their case). This way, it is possible to optimize the waveguide design for octave-spanning supercontinuum. Interestingly, they also showed a drastic pulse compression, resulting in a short pulse with a duration of approximately 10 fs. Such a supercontinuum source on the SOI platform is of prime interest for optical communication applications, offering the possibility to generate a stable frequency comb suitable for wavelength division multiplexing, and also for frequency metrology or pulse compression. In 2018, the first experimental demonstration of a coherent octave-spanning supercontinuum on the SOI platform in the near-IR range was reported by pumping a rib waveguide at a wavelength of 1.9 μm [39]. At this wavelength, TPA is still present, but its effect is reduced compared to shorter wavelengths while the nonlinear index is higher, and the waveguide profile is tailored to exhibit anomalous dispersion. This optimization improves the overall nonlinear behavior of the waveguide, enabling the generation of a broadband coherent supercontinuum extending from 1 to 2.4 μm when pumped by a pulsed laser with a duration between 50 and 100 fs, a coupled average power of 3.6 mW, and a repetition rate of 200 MHz. Moreover, they experimentally measured the coherence of the spectrum, showing a degree of mutual coherence higher than 95% over the whole bandwidth, allowing f-to-$2f$ interference for self-referencing of the frequency comb. Figures 4(a) and 4(d) show the geometry of the waveguide and the associated supercontinuum spectrum with its degree of coherence. Recently, the same group showed the possibility of improving the generated spectrum shape by use of Bragg gratings [42]. This method permits one to greatly enhance the generation in low-power spectral regions, which can be a way to generate flatter spectra. These studies show that despite the presence of TPA in Si in the near-IR range and the low upper bound of transparency of SiO_2, it is still possible to perform coherent octave-spanning SCG on the SOI platform in the near-IR range.

B. Mid-IR SCG Demonstrations in Si

In order to avoid TPA, it is interesting to work further in the mid-IR domain. Results on SOI were obtained by designing the waveguide cross section so that it operates in the anomalous dispersion regime at wavelengths higher than 2.2 μm, where TPA vanishes. However, the upper limit of the spectrum bandwidth stays limited due to absorption in the BOX layer. To overcome this limitation, researchers investigated other solutions by replacing the SiO_2 layer with different materials exhibiting a wider transparency window. In 2015, Singh *et al.* proposed using sapphire as a substrate, which is transparent up to 6 μm [43]. Thanks to this approach, they achieved the widest SCG in Si waveguides at that time, extending from 1.9 to 6 μm. To obtain this result, they pumped a strip waveguide of a cross section 2400 nm × 480 nm with a 320 fs pulsed source centered at 3.7 μm with a repetition rate of 20 MHz and a peak power up to 2.5 kW. More recently, in 2018, Nader *et al.* reported mid-IR dual-comb spectroscopy

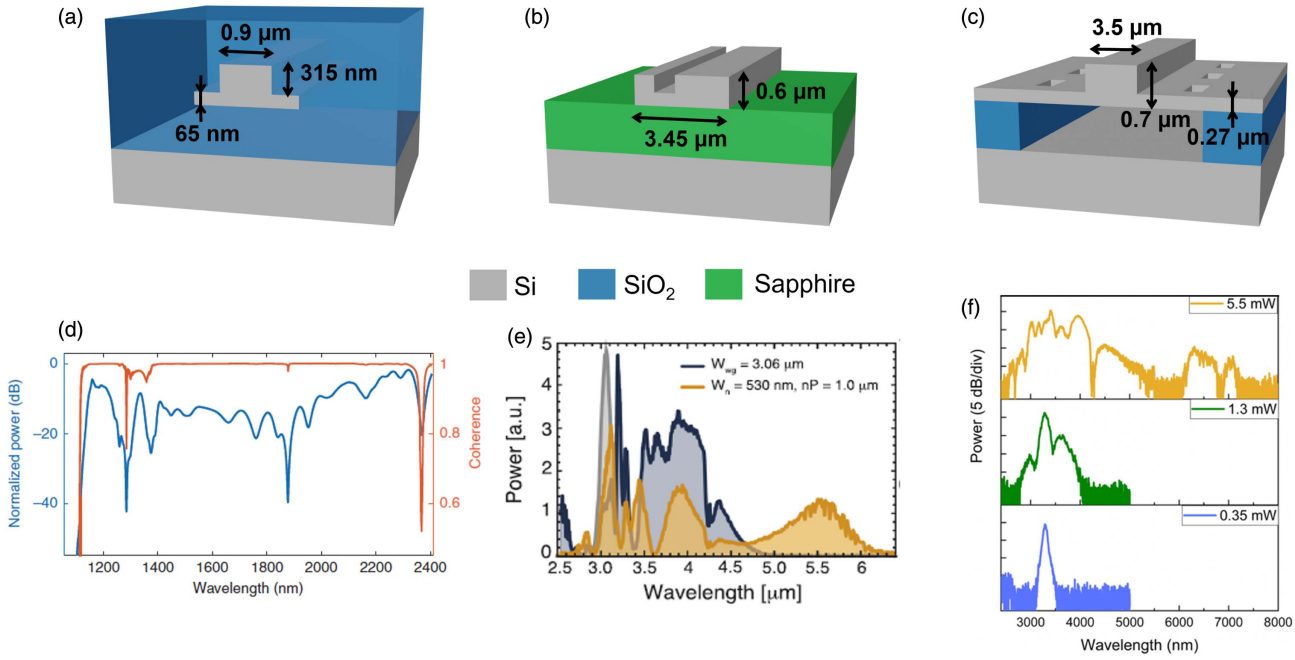

Fig. 4. Examples of SCG results in Si waveguides. Top row shows the schematic representations of the waveguide geometries; bottom row shows the corresponding results (spectra). (a) and (d) SOI platform, from Ref. [39]; (b) and (e) Si on sapphire platform, from Ref. [40]; (c) and (f) suspended Si waveguide [41].

on a gas sample using Si-on-sapphire (SOS) waveguides based on SCG covering wavelengths from 2.5 to 6.2 μm through the use of notch waveguides, a design that provides more degrees of freedom for dispersion engineering than simple strip waveguides [40] [Figs. 4(b) and 4(e)]. The center wavelength was chosen to be 3.06 μm, using a source with a pulse duration of 100 fs, a coupled average power of 12 mW, and a repetition rate of 100 MHz. These demonstrations show promising possibilities of the Si-on-sapphire platform for SCG, but fabrication techniques still need to be improved to reduce propagation losses caused by lattice mismatch between Si and sapphire, which are still in the order of 5 dB/cm.

Another solution to remove the barrier caused by the absorption in the bottom cladding is to use suspended Si waveguides. In these structures, the BOX is removed around the waveguide's core, which is then surrounded only by air, as shown in Fig. 4(c). This approach offers two main advantages: it totally removes the issue of material absorption in the BOX, and it increases the confinement of light in the Si core, enhancing the nonlinear effect. This platform is more challenging in terms of fabrication, as it requires precise selective etching of the BOX and specific design of the Si core to create the suspended structure, but it also shows great advantages for SCG. In 2018, Kou *et al.* realized Si suspended waveguides designed in order to exhibit anomalous dispersion around a wavelength of 4 μm [44]. They pumped 7 to 12 mm long waveguides with 300 fs short optical pulses and a few microwatts of average power coupled in the waveguides and a repetition rate of 150 kHz. They obtained a spectrum covering a wide range of wavelength from 2 to 5 μm, which can be used for absorption spectroscopy, for example. For instance, their experiment results clearly show the absorption of CO_2 at ∼4.25 μm. Later, in 2019, there was also a demonstration of coherent SCG in a suspended Si waveguide fabricated through wafer bonding to create the suspended structure [45]. They measured a wider spectrum (2 to 7.7 μm) by pumping the waveguide at a wavelength of 3.06 μm with 85 fs pulses and a coupled peak power of 1.1 kW. They used it to perform dual-comb spectroscopy of atmospheric water vapor, methanol, and isopropanol, giving results in excellent agreement with the predicted absorption spectra and performances at the level of current state-of-the-art devices. Very recently, similar results in terms of bandwidth were obtained with suspended Si waveguides fabricated with more standard wet-etching techniques instead of complex wafer bonding methods [Fig. 4(f)] [41].

C. Novel Waveguide Designs

In the results presented in the previous sections, the waveguides consist in fixed width Si channels. Recently, new routes have been explored to enhance SCG performance using more complex designs. Indeed, SCG is strongly dependent on the dispersion, which is very sensitive to the waveguide's geometry. Therefore, by implementing a variation of the waveguide's width, it is possible to generate different solitons and DWs along propagation. In 2017, Ciret and Gorza numerically investigated such varying width structures and showed that the SCG process leads to broader, flatter, and more coherent spectra [46]. In 2019, Singh *et al.* proposed three varying dispersion designs: two-section and three-section cascaded waveguides

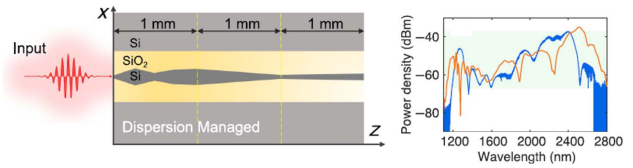

Fig. 5. SCG in dispersion-managed waveguides, from Ref. [48] with the permission of APS Physics, Copyright (2018) by the American Physical Society.

(discrete variation of width), and tapers (continuously varying width) [47]. In all the cases, they experimentally showed that the supercontinuum is broader and flatter than in single-width configurations, as predicted by the numerical work of Ciret and Gorza, and the coherence is greatly enhanced, in particular for the taper waveguides, since MI cannot build up efficiently in such a structure. Soon after these promising results, Wei *et al.* proposed a similar approach based on cascaded waveguides [48]. The design they propose contains seven sections. The determination of the widths, lengths, and positions of each section was optimized by the use of a genetic algorithm made to produce broad and flat spectra, as depicted in Fig. 5. They obtained quite flat supercontinuum spectra covering the whole transmission window of the waveguides with a high degree of coherence all over the bandwidth, with a low input pulse energy (∼0.9 pJ).

Also, it is well known that the effect of noise through the MI process is higher for longer pulses. The use of ultrashort femtosecond pulses is advantageous for SCG but represents a greater challenge for integration using mode-locked lasers. Cheng *et al.* proposed a design composed of a tapered waveguide optimized for pulse compression, followed by a fixed width section designed for efficient SCG [49]. This technique permits one to use picosecond pulses at the input of the waveguide, which are then compressed into femtosecond pulses by the tapered region, which gives a more appropriate condition for SCG in the following section of the waveguide.

Of course, the methods proposed in these studies are not restricted to Si waveguides, and they can be transposed to any platform. These novel results show very promising perspectives for SCG optimization in integrated waveguides.

5. SCG IN Ge-BASED DEVICES

The use of Si waveguides for mid-IR applications restricts the upper bound of the spectrum to 8.5 μm. To obtain SCG at higher wavelengths, solutions are investigated through the use of Ge and SiGe alloys, as Ge is transparent from 1.5 up to 14.5 μm [35]. Moreover, Ge is compatible with Si technology, and it has a nonlinear index 1 order of magnitude higher than that of Si (see Fig. 3), making it an excellent candidate for broadband integrated mid-IR supercontinuum sources.

Very recently, SCG was obtained in pure Ge waveguides grown on Si [50]. The use of pure Ge permits one to benefit from the high nonlinear index of the material and its full transparency range, but the lattice mismatch between Si and Ge results in dislocations responsible for propagation loss. In this

study, an optimized fabrication process based on epitaxial growth enabled the researchers to strongly reduce the threading dislocation density and to reach linear propagation losses of 1.2 dB/cm. They were able to generate a supercontinuum from 3.4 to 6 μm with a pump wavelength of 4.6 μm, 200 fs duration, up to 22 mW of average coupled power, and a repetition rate of 63 MHz. The limitation in the long wavelength side is attributed to high free-carrier loss, and the authors anticipate that this issue can be overcome by pumping the waveguide at a higher wavelength. Nevertheless, the broadest SCG results were found using SiGe alloys. $Si_{1-x}Ge_x$ combinations have the advantage of reducing dislocations, and so to decrease linear losses. The same group presented results in a SiGe on Si waveguide with 40% of Ge, exhibiting lower propagation losses of 0.23 dB/cm [51]. With the same platform, they also achieved broad all-normal dispersion SCG (from 2.8 to 5.7 μm) [52]. While the spectral broadening is lower than in the anomalous dispersion case, the output spectrum presents a flat, smooth shape and high coherence, as expected when pumping in the normal dispersion regime, and allows one to compress the 200 fs pulse down to 22 fs. However, this platform encounters some inconvenience: the Si substrate imposes the upper limit of the spectrum to approximately 8.5 μm, and the increase of Ge concentration for better confinement and nonlinearity would be at the cost of threading dislocation density responsible for higher losses. Another approach is based on a graded index SiGe alloy. This platform consists in a waveguide presenting a linearly increasing Ge concentration in the SiGe core along the vertical axis, reaching a value of 80% [53]. This way, a high concentration of Ge can be achieved with few dislocations. Moreover, with such a technique, the optical mode is confined in the upper part of the waveguide, where the refractive index is higher due to the high Ge concentration, far away from the Si substrate. The geometry of the waveguide is described in Fig. 6(a). Consequently, this platform avoids absorption losses in the substrate at wavelengths higher than 8.5 μm. Propagation losses were measured to be at decibel per centimeter levels at long wavelengths (up to 9.5 μm), and the nonlinear parameter γ is estimated to be around 1 $W^{-1}\,m^{-1}$ at a wavelength of 5 μm and 0.5 $W^{-1}\,m^{-1}$ at 8 μm. The quite low nonlinear parameter compared to what is usually observed in Si waveguides despite a higher nonlinear index of Ge is due

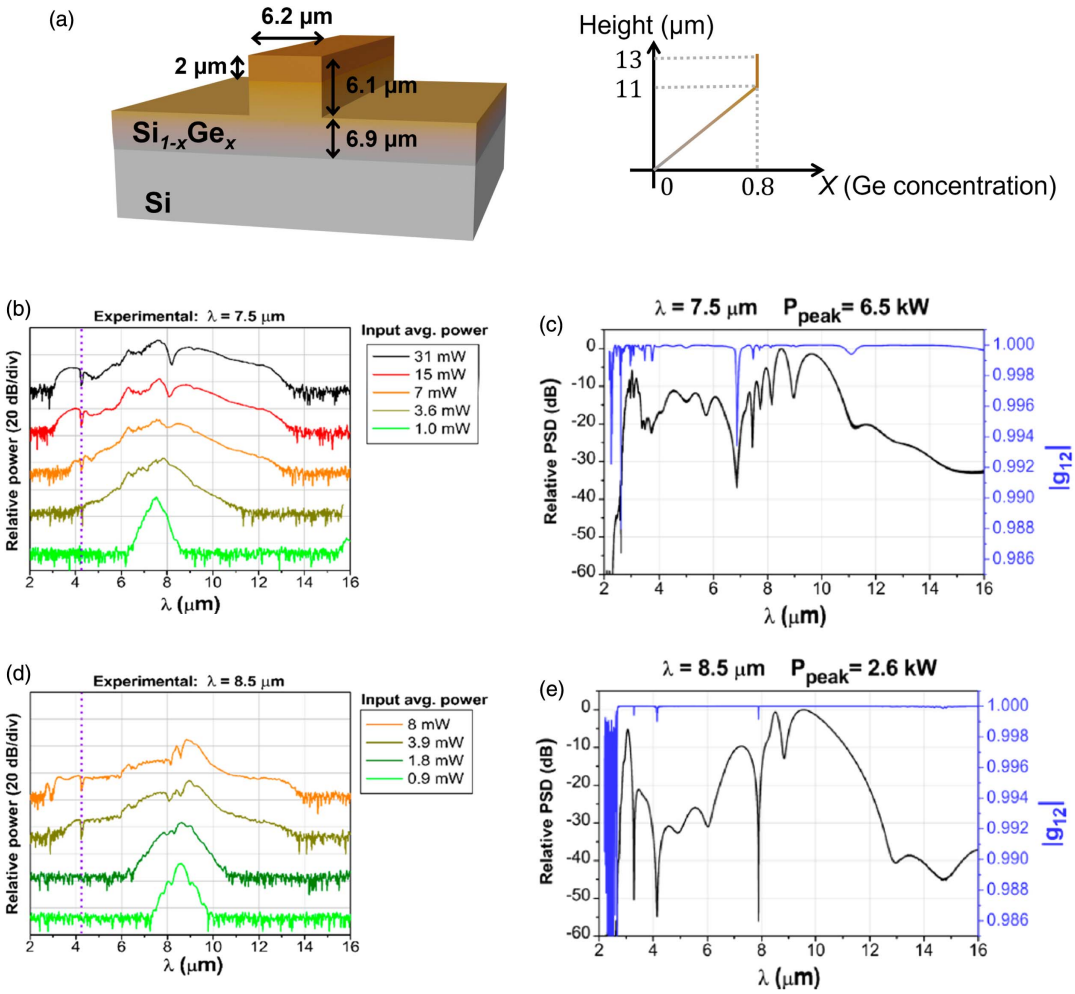

Fig. 6. Results on the graded SiGe platform, from Ref. [53]. (a) Schematic representation of the waveguide geometry with the linearly increasing Ge concentration profile along the vertical axis; (b) and (c) experimental and simulated (spectral density in black, coherence in blue) results for a pump wavelength of 7.5 μm, respectively. The purple dashed line shows the dip due to CO_2 absorption. (d) and (e) Experimental and simulated results for a pump wavelength of 8.5 μm, respectively.

to a high effective modal area and the high wavelength in mid-IR operation. By dispersion engineering, anomalous dispersion is obtained at long wavelengths, and extremely broad supercontinua were measured, covering more than two octaves from 3 to 13 μm. The waveguide was pumped with 200 fs pulses and the wide anomalous dipsersion region permitted one to vary the pump wavelength and study its effect, showing that broad SCG can be obtained on a wide range of pump wavelengths [Figs. 6(b) and 6(d)]. As far as we know, this result evidences the longest wavelengths obtained with SCG in a Si-compatible integrated photonic platform. Furthermore, numerical simulations show a high degree of coherence over the entire bandwidth of the spectrum, as shown in Figs. 6(c) and 6(e). This progress in the mid-IR range points toward a promising future for Ge-based waveguides for nonlinear applications in imaging, spectroscopy, or free-space communications.

6. SCG IN SiN_x-BASED DEVICES

As seen in the previous sections, the main obstacles of Si photonics for SCG in the near-IR range are TPA and linear absorption. The SiN_x platform has been intensively studied as a solution that overcomes both matters. Indeed, SiN_x has a high bandgap, corresponding to an absorption edge in the deep-UV region (~230 nm). As a consequence, TPA only occurs in the UV and a part of visible ranges. In addition, the transparency window of this material extends up to 7 μm. Also, fabrication processes of SiN_x films via chemical vapor deposition techniques are very mature and are compatible with Si technology. This makes SiN_x a viable candidate for SCG in the visible, near-IR, and partially mid-IR ranges. As for the nonlinear index, it is difficult to give a precise value, as it strongly depends on the stoichiometry: a higher Si/N ratio results in a higher nonlinear index [54]. Nevertheless, a value of $n_{2,SiN} \sim 2.4 \times 10^{-19}$ m^2/W is usually considered for stoichiometric Si_3N_4 in the near-IR region. This value is 1 order of magnitude lower than that of Si (see Fig. 3), but it is still high enough to achieve efficient nonlinear processes in integrated devices. Indeed, the extremely low propagation losses achieved in the SiN_x platform, even lower than 1 dB/cm, make it possible to work with long structures, increasing the nonlinear interactions in the waveguide, and hence compensating for its reduced nonlinear index. Moreover, the ease of tuning the Si/N ratio during deposition enables wide possibilities to tailor the properties of the material. Eventually, the large transparency window, low temperature sensitivity, ease of fabrication, and good nonlinear properties make SiN_x a particularly interesting choice for integrated nonlinear photonics compatible with Si technology.

A tremendous number of publications about SCG in SiN_x have been published in the last few years, showing important progress. In particular, fabrication techniques to obtain high-quality films were established with two main objectives: to reduce propagation losses as much as possible, and to improve the compatibility with Si fabrication process flows [55–59]. Methods to deposit crack-free SiN_x films have been reported, resulting in subdecibel per centimeter propagation loss in waveguides. While being extremely interesting for the exploitation of efficient nonlinear processes, these methods are only compatible with front-end-of-line (FEOL) CMOS process flows due to a high thermal budget that hinders the cointegration of photonic devices with electronic components. Therefore, efforts were also made to find ways to deposit SiN_x with low temperature so that the technique could be compatible with back-end-of-line (BEOL) CMOS process flows.

From the significant interest allocated to SCG in SiN_x waveguides, many demonstrations of impressive results and novel devices have been published in the last several years [25,60–66]. Ultrabroadband SCG has been measured covering more than two octaves, including the visible range and the near-IR range [67–69]. For example, we experimentally and numerically studied SCG in low-loss (<1 dB/cm) nitrogen-rich SiN_x waveguides, extending from 400 up to 1600 nm (Fig. 7). The 600 nm × 1200 nm waveguides were pumped at a center wavelength of 1.2 μm, with pulses with 130 fs duration, an average coupled power of a few microwatts, and a repetition rate of 1 MHz. The extensive amount of nitrogen in the film was made on purpose in order to reduce the refractive index of the material for better compatibility with fiber-to-chip coupling schemes in the O-band optical communication window (around a wavelength 1330 nm). Dispersion engineering permitted researchers to obtain a wide anomalous dispersion region that led to the extremely broad supercontinuum spectrum. This result also shows the important part

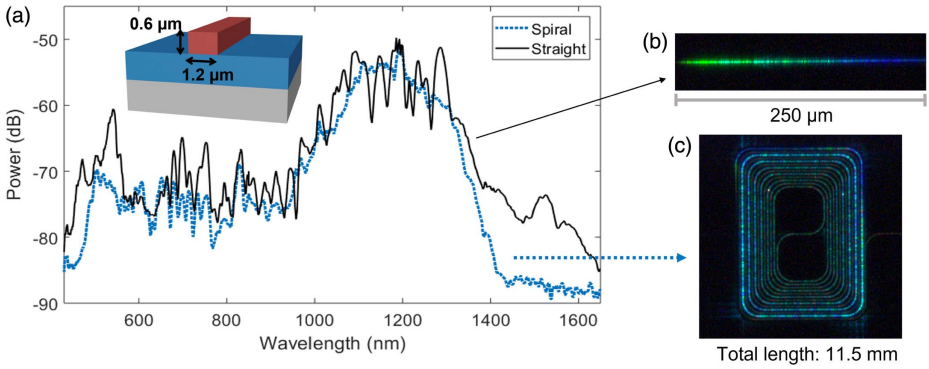

Fig. 7. Two octaves spanning SCG in nitrogen-rich SiN_x waveguides, from Ref. [67]. (a) Output spectra of spiral and straight waveguides. Inset schematically shows the geometry of the air-clad waveguide. (b) and (c) Top view optical images of the straight waveguide and the spiral waveguide, respectively, showing light generation in the visible range.

played by dispersion engineering. Indeed, while the nonlinear parameter of the waveguide is 2 orders of magnitude lower than what can be obtained in Si-rich SiN_x waveguides, the bandwidth is higher than results in these waveguides, only thanks to a different dispersion profile that covers a broad region and allows for the existence of two DWs that are far away from each other. Furthermore, it is clearly visible in Fig. 7 that the long spiral waveguide exhibits much lower power after 1400 nm than the short straight waveguide. This highlights the influence of losses in the SCG process. Indeed, this difference of power level comes from absorption losses in a region around a wavelength of 1500 nm due to N-H bonds in the SiN_x film. The extension of the spectrum in the visible region also makes it interesting for biosensing, for example. Numerical results also show the ability to generate such a spectrum with a high coherence, near unity over the whole bandwidth.

SiN_x waveguides with ultralow loss, under 1 dB/cm, were used to generate light in the mid-IR region up to 4 μm through DW generation with a high conversion efficiency, giving microwatt levels of output power [70]. The efficient conversion of near-IR light into the mid-IR domain is a very appealing approach, and dispersion engineering of low-loss SiN_x waveguides appears to be a promising solution. The same waveguide was then used to demonstrate gas spectroscopy, showing excellent agreement with the theoretical absorption spectra of the tested chemical compounds. Moreover, it was reported that performances of mid-IR dual-comb spectroscopy based on SCG can be enhanced with supermode dispersion engineering in a coupled waveguide [71]. In this study, the use of coupled waveguides offers new advantages to tailor the dispersion and to enhance mid-IR light generation.

Recently, the same group also reported SCG in a SiN_x waveguide with a strong dependence on polarization [72]. The waveguide exhibits opposite GVD for each polarization (transverse electric, TE and transverse magnetic, TM) at a wavelength of 2.1 μm: the TE mode experiences anomalous dispersion leading to an octave-spanning SCG based on soliton fission, whereas the TM mode lies within the normal dispersion regime that results in flat and smooth SPM-driven SCG suitable for postcompression of the pulse for few-cycle pulse generation. This result unveils the versatility of such an approach, showing the possibility to choose between the types of SCG mechanisms only by switching the input polarization, depending on the desired application.

In 2018, a fully self-referenced frequency comb with low electrical power requirements based on SCG in a SiN_x waveguide was reported [73]. Such an achievement shows the high potential of the SiN_x platform for applications based on SCG using low-cost integrated photonic chips.

7. DISCUSSION

A high variety of waveguides have been studied for integrated SCG in different wavelength windows. These works show the high potential of Si-compatible platforms for nonlinear applications. As seen in the literature, the most developed applications of integrated SCG at the moment are related to sensing, with impressive results in dual-comb spectroscopy, for example. This application is the most straightforward for SCG, as it does not require unreasonable complexity of the devices and is well adapted for on-chip integration, since the whole system can be built at the same time on the same chip. However, integrated SCG devices currently suffer from an important weakness: the pump laser source. Indeed, most of the studies performed on integrated SCG are done using high volume, expensive pulsed lasers, and optical parametric amplifiers, which is contrary to the initial goal of building compact and cost-efficient nonlinear devices. For example, using an SCG chip for an imaging system would not be so beneficial if it still needed a dedicated fiber-pulsed laser and an optical parametric amplifier. Additionally, while many publications mention optical communications among the potential applications of SCG, it is currently not viable, especially due to the pump repetition rate requirements: all the work presented here is done with sources of quite low repetition rates (in the megahertz range), while even dense wavelength division multiplexing systems use at least 12.5 GHz channel spacing, several orders of magnitude higher than the frequency spacing of the SCG-based combs cited here. In the end, the production of high bandwidth and coherent spectra through SCG puts colossal constraints on the initial light source: high peak power (often in the order of several kilowatts), very short pulses (in the order of a few hundreds of femtoseconds), high repetition rate (more than 10 GHz), and ideally low relative intensity noise. While the final goal would be to achieve SCG with integrated mode-locked lasers, it appears incredibly challenging to achieve such performance at the moment. Nevertheless, in our opinion, the development of novel designs and the rapid evolution of laser technologies go toward the fulfillment of this challenge in the future. For instance, the implementation of a pulse compression stage before the waveguide designed for SCG is an interesting approach to lighten the requirements on the duration and the peak power of the initial pulse; the use of tapered waveguides allows one to reduce the sensitivity to MI triggered by noise, hence reducing the phase and intensity fluctuations of the generated spectrum, and advances in light-coupling schemes permit one to drastically reduce losses at the input and output of the waveguides. Moreover, mode-locked laser chips also have seen some progress, with demonstrations of integrated sources with subpicosecond short pulses and repetition rates between 10 and 100 GHz [74]. The peak power of such laser diodes remains rather low (in the order of a few milliwatts up to 1 W) compared to the needs for SCG, meaning that amplifiers may be necessary. Yet, the progress made in the design of waveguides for SCG and in the laser technologies leads us to believe that compact nonlinear devices still have a bright future.

8. CONCLUSION

Diverse photonics platforms compatible with Si technology have been studied during the past two decades to develop on-chip SCG. Performance has not stopped improving; ways to overcome obstacles such as substrate absorption, TPA, or fabrication complexity have been implemented. A summary of SCG performance in Si-compatible platforms is given in Table 1. Si waveguides proved to be suitable for near-IR and mid-IR SCG. To obtain supercontinuum spectra extending farther in the long wavelength side, germanium-based

Table 1. Main Parameters of the Different Platforms for SCG Presented in the Review[a]

Platform	Transparency window (μm)	α (dB/cm)	γ (W^{-1} m^{-1})	Bandwidth observed (μm)	Pulse duration (fs)	Peak power (W)	Reference
SOI	1.2–4	N/A	220	1.1–2.8	70	11	[48]
		~1.5 (1.9 μm)	140	1.06–2.4	~50	~320	[39]
SOS	1.2–6	~5 (3.7 μm)	~10	2–6	320	1820	[43]
Suspended Si	1.2–8	~2 (3.2 μm)	~10	2.5–7	220	N/A	[41]
		~5 (4 μm)	N/A	2–5	300	42,000	[44]
SiGe	1.8–14	~0.5 (8 μm)	~0.5	3–13	220	2600	[53]
		~1 (4.6 μm)	~1.6	3.39–6.2	200	3300	[50]
SiN_x	0.25–4	~0.5 (1.3 μm)	~1	0.4–1.6	130	3800	[67]
		~0.5 (1.56)	~1	0.53–2.6	120	~17,000	[69]
		~0.2 (2.09)	N/A	1.3–4	78	6800	[70]

[a]In column 3, the number in parentheses is the corresponding wavelength for the value of α.

waveguides were envisaged, and outstanding results were observed, both with standard Ge and SiGe alloy waveguides. Also, SiN_x has been extensively studied, as it provides a high potential platform for nonlinear applications. Indeed, it does not suffer from TPA in the optical communication windows, it has a large transparency window, and it offers additional degrees of freedom to play on nonlinearity and dispersion. Many results were published, demonstrating state-of-the-art performance in spectroscopy or in self-referenced frequency combs for optical communications or frequency metrology, for example. Thanks to these studies, it was possible to precisely understand how SCG is formed in integrated waveguides and how to optimize it. Consequently, more complex novel designs are now being investigated to pursue the development of low-cost, highly efficient integrated platforms for SCG.

Funding. Réseau RENATECH; Conseil Départemental de l'Essonne; Ministère de l'Économie, des Finances et de l'Industrie (Nano2022 IPCEI); Agence Nationale de la Recherche (ANR-17-CE09-0041, ANR-19-CE24-0002-01); H2020 European Research Council (639107, 647342).

Acknowledgment. Frédéric Boeuf, Stéphane Monfray, and Charles Baudot from STMicroelectronics and Sylvain Guerber, Quentin Wilmart, and Bertrand Szelag from CEA-Leti are acknowledged for fruitful discussions and fabrication contribution in SiN_x. Jacopo Frigerio and Giovanni Isella from Politecnico di Milano are also acknowledged for the SiGe alloy epitaxial growth. All engineers in the C2N cleanroom (PIMENT platform) and especially Jean-René Coudevylle, Etienne Herth, David Bouville, Nathalie Isac, Samson Edmond, and Cédric Villebasse are acknowledged for their fabrication contribution. The fabrication of some reported devices was partially carried out at the Micro-NanoTechnologie platform/C2N, which was partially funded by the Conseil Général de l'Essonne. This work was also partly supported by the French RENATECH network.

Disclosures. The authors declare no conflicts of interest.

Data Availability. No data were generated or analyzed in the presented research.

REFERENCES

1. P. A. Franken, A. E. Hill, C. W. Peters, and G. Weinreich, "Generation of optical harmonics," Phys. Rev. Lett. **7**, 118–119 (1961).
2. F. Biancalana, D. V. Skryabin, and A. V. Yulin, "Theory of the soliton self-frequency shift compensation by the resonant radiation in photonic crystal fibers," Phys. Rev. E **70**, 016615 (2004).
3. Z. Zhu and T. G. Brown, "Effect of frequency chirping on supercontinuum generation in photonic crystal fibers," Opt. Express **12**, 689–694 (2004).
4. J. M. Dudley, G. Genty, and S. Coen, "Supercontinuum generation in photonic crystal fiber," Rev. Mod. Phys. **78**, 1135–1184 (2006).
5. G. Humbert, W. J. Wadsworth, S. G. Leon-Saval, J. C. Knight, T. A. Birks, P. S. J. Russell, M. J. Lederer, D. Kopf, K. Wiesauer, E. I. Breuer, and D. Stifter, "Supercontinuum generation system for optical coherence tomography based on tapered photonic crystal fibre," Opt. Express **14**, 1596–1603 (2006).
6. A. Mussot, M. Beaugeois, M. Bouazaoui, and T. Sylvestre, "Tailoring CW supercontinuum generation in microstructured fibers with two-zero dispersion wavelengths," Opt. Express **15**, 11553–11563 (2007).
7. L. Graini and K. Saouchi, "80 Gb/s WDM communication system based on spectral slicing of continuum generating by chirped pulse propagation in law normal dispersion photonic crystal fiber," in *Modeling Approaches and Algorithms for Advanced Computer Applications*, A. Amine, A. M. Otmane, and L. Bellatreche, eds., Studies in Computational Intelligence (Springer, 2013), pp. 217–225.
8. H. Saghaei, "Supercontinuum source for dense wavelength division multiplexing in square photonic crystal fiber via fluidic infiltration approach," Radioengineering **26**, 16–22 (2017).
9. M. Veljkovic, D. Milovic, A. Maluckov, A. Biswas, F. B. Majid, and C. M. Glenn, "Chaotic dynamics and supercontinuum generation with cosh-Gaussian pulses in photonic-crystal fibers," Laser Phys. **28**, 095109 (2018).
10. C. Kaminski, R. Watt, A. Elder, J. Frank, and J. Hult, "Supercontinuum radiation for applications in chemical sensing and microscopy," Appl. Phys. B **92**, 367–378 (2008).
11. L. Deniel, M. Gay, D. P. Galacho, C. Baudot, L. Bramerie, O. Ozolins, F. Boeuf, L. Vivien, C. Peucheret, and D. Marris-Morini, "DAC-less PAM-4 generation in the O-band using a silicon Mach-Zehnder modulator," Opt. Express **27**, 9740–9748 (2019).
12. D. González-Andrade, C. Lafforgue, E. Durán-Valdeiglesias, X. Le Roux, M. Berciano, E. Cassan, D. Marris-Morini, A. V. Velasco, P. Cheben, and L. Vivien, "Polarization- and wavelength-agnostic nanophotonic beam splitter," Sci. Rep. **9**, 3604 (2019).
13. D. Oser, D. Pérez-Galacho, X. L. Roux, S. Tanzilli, L. Vivien, L. Labonté, E. Cassan, and C. Alonso-Ramos, "Silicon subwavelength modal Bragg grating filters with narrow bandwidth and high optical rejection," Opt. Lett. **45**, 5784–5787 (2020).
14. D. González-Andrade, D. Pérez-Galacho, M. Montesinos-Ballester, X. L. Roux, E. Cassan, D. Marris-Morini, P. Cheben, P. Cheben, N. Vulliet, and S. Monfray, "Dual-band fiber-chip grating coupler in

a 300 mm silicon-on-insulator platform and 193 nm deep-UV lithography," Opt. Lett. **46**, 617–620 (2021).
15. D. Benedikovic, L. Virot, G. Aubin, J.-M. Hartmann, F. Amar, X. Le Roux, C. Alonso-Ramos, E. Cassan, D. Marris-Morini, and P. Crozat, "40 Gbps heterostructure germanium avalanche photo receiver on a silicon chip," Optica **7**, 775–783 (2020).
16. K. Shi, S. H. Nam, P. Li, S. Yin, and Z. Liu, "Wavelength division multiplexed confocal microscopy using supercontinuum," Opt. Commun. **263**, 156–162 (2006).
17. N. M. Israelsen, C. R. Petersen, A. Barh, D. Jain, M. Jensen, G. Hannesschläger, P. Tidemand-Lichtenberg, C. Pedersen, A. Podoleanu, and O. Bang, "Real-time high-resolution mid-infrared optical coherence tomography," Light Sci. Appl. **8**, 11 (2019).
18. S. Rao, M. Jensen, L. Grüner-Nielsen, J. T. Olsen, P. Heiduschka, B. Kemper, J. Schnekenburger, M. Glud, M. Mogensen, and N. M. Israelsen, "Shot-noise limited, supercontinuum-based optical coherence tomography," Light Sci. Appl. **10**, 133 (2021).
19. D. P. Popescu, L.-P. Choo-Smith, C. Flueraru, Y. Mao, S. Chang, J. Disano, S. Sherif, and M. G. Sowa, "Optical coherence tomography: fundamental principles, instrumental designs and biomedical applications," Biophys. Rev. **3**, 155–169 (2011).
20. Z. Yaqoob, J. Wu, and C. Yang, "Spectral domain optical coherence tomography: a better OCT imaging strategy," BioTechniques **39**, S6–S13 (2005).
21. L. Boivin and B. C. Collings, "Spectrum slicing of coherent sources in optical communications," Opt. Fiber Technol. **7**, 1–20 (2001).
22. T. Ohara, H. Takara, T. Yamamoto, H. Masuda, T. Morioka, M. Abe, and H. Takahashi, "Over-1000-channel ultradense WDM transmission with supercontinuum multicarrier source," J. Lightwave Technol. **24**, 2311–2317 (2006).
23. C. Ware, S. Cordette, C. Lepers, I. Fsaifes, B. Kibler, C. Finot, and G. Millot, "Spectral slicing of a supercontinuum source for WDM/DS-OCDMA application," in *10th Anniversary International Conference on Transparent Optical Networks* (IEEE, 2008), pp. 158–161.
24. R. Wu, V. Torres-Company, D. E. Leaird, and A. M. Weiner, "Supercontinuum-based 10-GHz flat-topped optical frequency comb generation," Opt. Express **21**, 6045–6052 (2013).
25. D. R. Carlson, D. D. Hickstein, A. Lind, J. B. Olson, R. W. Fox, R. C. Brown, A. D. Ludlow, Q. Li, D. Westly, H. Leopardi, T. M. Fortier, K. Srinivasan, S. A. Diddams, and S. B. Papp, "Photonic-chip supercontinuum with tailored spectra for counting optical frequencies," Phys. Rev. Appl. **8**, 014027 (2017).
26. C.-S. Brès, "With a fine-tooth comb," Nat. Phys. **16**, 600 (2020).
27. S. A. Diddams, D. J. Jones, J. Ye, S. T. Cundiff, J. L. Hall, J. K. Ranka, R. S. Windeler, R. Holzwarth, T. Udem, and T. W. Hänsch, "Direct link between microwave and optical frequencies with a 300 THz femtosecond laser comb," Phys. Rev. Lett. **84**, 5102–5105 (2000).
28. R. W. Boyd, *Nonlinear Optics*, 3rd ed. (Academic, 2008).
29. G. Agrawal, *Nonlinear Fiber Optics*, 6th ed. (Academic, 2019).
30. F. Lu and W. H. Knox, "Generation of a broadband continuum with high spectral coherence in tapered single-mode optical fibers," Opt. Express **12**, 347–353 (2004).
31. E. Treacy, "Optical pulse compression with diffraction gratings," IEEE J. Quantum Electron. **5**, 454–458 (1969).
32. D. Grischkowsky and A. C. Balant, "Optical pulse compression based on enhanced frequency chirping," Appl. Phys. Lett. **41**, 1–3 (1982).
33. C. Finot, B. Kibler, L. Provost, and S. Wabnitz, "Beneficial impact of wave-breaking for coherent continuum formation in normally dispersive nonlinear fibers," J. Opt. Soc. Am. B **25**, 1938–1948 (2008).
34. Y. Kodama and A. Hasegawa, "Nonlinear pulse propagation in a monomode dielectric guide," IEEE J. Quantum Electron. **23**, 510–524 (1987).
35. L. Zhang, A. M. Agarwal, L. C. Kimerling, and J. Michel, "Nonlinear group IV photonics based on silicon and germanium: from near-infrared to mid-infrared," Nanophotonics **3**, 247–268 (2014).
36. I.-W. Hsieh, X. Chen, X. Liu, J. I. Dadap, N. C. Panoiu, C.-Y. Chou, F. Xia, W. M. Green, Y. A. Vlasov, and R. M. Osgood, "Supercontinuum generation in silicon photonic wires," Opt. Express **15**, 15242–15249 (2007).
37. L. Yin, Q. Lin, and G. P. Agrawal, "Soliton fission and supercontinuum generation in silicon waveguides," Opt. Lett. **32**, 391–393 (2007).
38. L. Zhang, Q. Lin, Y. Yue, Y. Yan, R. G. Beausoleil, and A. E. Willner, "Silicon waveguide with four zero-dispersion wavelengths and its application in on-chip octave-spanning supercontinuum generation," Opt. Express **20**, 1685–1690 (2012).
39. N. Singh, M. Xin, D. Vermeulen, K. Shtyrkova, N. Li, P. T. Callahan, E. S. Magden, A. Ruocco, N. Fahrenkopf, C. Baiocco, B. P.-P. Kuo, S. Radic, E. Ippen, F. X. Kärtner, and M. R. Watts, "Octave-spanning coherent supercontinuum generation in silicon on insulator from 1.06 μm to beyond 2.4 μm," Light Sci. Appl. **7**, 17131 (2018).
40. N. Nader, D. L. Maser, F. C. Cruz, A. Kowligy, H. Timmers, J. Chiles, C. Fredrick, D. A. Westly, S. W. Nam, R. P. Mirin, J. M. Shainline, and S. Diddams, "Versatile silicon-waveguide supercontinuum for coherent mid-infrared spectroscopy," APL Photon. **3**, 036102 (2018).
41. T. T. D. Dinh, X. Le Roux, M. Montesinos-Ballester, C. Lafforgue, E. Cassan, D. Marris-Morini, L. Vivien, and C. Alonso-Ramos, "Internal work from the minaphot team at c2n," unpublished (2021).
42. N. Singh, M. Raval, E. Ippen, M. R. Watts, and F. X. Kärtner, "Supercontinuum generation in silicon Bragg grating waveguide," Appl. Phys. Lett. **118**, 071106 (2021).
43. N. Singh, D. D. Hudson, Y. Yu, C. Grillet, S. D. Jackson, A. Casas-Bedoya, A. Read, P. Atanackovic, S. G. Duvall, S. Palomba, B. Luther-Davies, S. Madden, D. J. Moss, and B. J. Eggleton, "Midinfrared supercontinuum generation from 2 to 6 μm in a silicon nanowire," Optica **2**, 797–802 (2015).
44. R. Kou, T. Hatakeyama, J. Horng, J.-H. Kang, Y. Wang, X. Zhang, and F. Wang, "Mid-IR broadband supercontinuum generation from a suspended silicon waveguide," Opt. Lett. **43**, 1387–1390 (2018).
45. N. Nader, A. Kowligy, J. Chiles, E. J. Stanton, H. Timmers, A. J. Lind, F. C. Cruz, D. M. B. Lesko, K. A. Briggman, S. W. Nam, S. A. Diddams, and R. P. Mirin, "Infrared frequency comb generation and spectroscopy with suspended silicon nanophotonic waveguides," Optica **6**, 1269–1276 (2019).
46. C. Ciret and S.-P. Gorza, "Generation of ultra-broadband coherent supercontinua in tapered and dispersion-managed silicon nanophotonic waveguides," J. Opt. Soc. Am. B **34**, 1156–1162 (2017).
47. N. Singh, D. Vermulen, A. Ruocco, N. Li, E. Ippen, F. X. Kärtner, and M. R. Watts, "Supercontinuum generation in varying dispersion and birefringent silicon waveguide," Opt. Express **27**, 31698–31712 (2019).
48. J. Wei, C. Ciret, M. Billet, F. Leo, B. Kuyken, and S.-P. Gorza, "Supercontinuum generation assisted by wave trapping in dispersion-managed integrated silicon waveguides," Phys. Rev. Appl. **14**, 054045 (2020).
49. Y. Cheng, J. Yuan, C. Mei, F. Li, Z. Kang, B. Yan, X. Zhou, Q. Wu, K. Wang, X. Sang, K. Long, C. Yu, and G. Farrell, "Self-similar picosecond pulse compression for supercontinuum generation at mid-infrared wavelength in silicon strip waveguides," Opt. Commun. **454**, 124380 (2020).
50. A. Della Torre, M. Sinobad, R. Armand, B. Luther-Davies, P. Ma, S. Madden, A. Mitchell, D. J. Moss, J.-M. Hartmann, V. Reboud, J.-M. Fedeli, C. Monat, and C. Grillet, "Mid-infrared supercontinuum generation in a low-loss germanium-on-silicon waveguide," APL Photon. **6**, 016102 (2021).
51. M. Sinobad, C. Monat, B. Luther-davies, P. Ma, S. Madden, D. J. Moss, A. Mitchell, D. Allioux, R. Orobtchouk, S. Boutami, J.-M. Hartmann, J.-M. Fedeli, and C. Grillet, "Mid-infrared octave spanning supercontinuum generation to 85 μm in silicon-germanium waveguides," Optica **5**, 360–366 (2018).
52. M. Sinobad, A. DellaTorre, R. Armand, B. Luther-Davies, P. Ma, S. Madden, A. Mitchell, D. J. Moss, J.-M. Hartmann, J.-M. Fedeli, C. Monat, and C. Grillet, "Mid-infrared supercontinuum generation in silicon-germanium all-normal dispersion waveguides," Opt. Lett. **45**, 5008–5011 (2020).
53. M. Montesinos-Ballester, C. Lafforgue, J. Frigerio, A. Ballabio, V. Vakarin, Q. Liu, J. M. Ramirez, X. L. Roux, D. Bouville, A. Barzaghi, C. Alonso-Ramos, L. Vivien, G. Isella, and D. Marris-Morini, "On-chip mid-infrared supercontinuum generation from 3 to 13 μm wavelength," ACS Photon. **7**, 3423–3429 (2020).
54. D. T. H. Tan, K. J. A. Ooi, and D. K. T. Ng, "Nonlinear optics on silicon-rich nitride—a high nonlinear figure of merit CMOS platform," Photon. Res. **6**, B50–B66 (2018).

55. T. Domínguez Bucio, A. Z. Khokhar, C. Lacava, S. Stankovic, G. Z. Mashanovich, P. Petropoulos, and F. Y. Gardes, "Material and optical properties of low-temperature NH_3-free PECVD SiN_x layers for photonic applications," J. Phys. D **50**, 025106 (2017).
56. J. Chiles, N. Nader, D. D. Hickstein, S. P. Yu, T. C. Briles, D. Carlson, H. Jung, J. M. Shainline, S. Diddams, S. B. Papp, S. W. Nam, and R. P. Mirin, "Deuterated silicon nitride photonic devices for broadband optical frequency comb generation," Opt. Lett. **43**, 1527–1530 (2018).
57. H. El Dirani, M. Casale, S. Kerdiles, C. Socquet-Clerc, X. Letartre, C. Monat, and C. Sciancalepore, "Crack-free silicon-nitride-on-insulator nonlinear circuits for continuum generation in the C-band," IEEE Photon. Technol. Lett. **30**, 355–358 (2018).
58. H. El Dirani, A. Kamel, M. Casale, S. Kerdiles, C. Monat, X. Letartre, M. Pu, L. K. Oxenløwe, K. Yvind, and C. Sciancalepore, "Annealing-free Si_3N_4 frequency combs for monolithic integration with Si photonics," Appl. Phys. Lett. **113**, 081102 (2018).
59. J. Liu, G. Huang, R. N. Wang, J. He, A. S. Raja, T. Liu, N. J. Engelsen, and T. J. Kippenberg, "High-yield, wafer-scale fabrication of ultralow-loss, dispersion-engineered silicon nitride photonic circuits," Nat. Commun. **12**, 2236 (2021).
60. A. R. Johnson, A. S. Mayer, A. Klenner, K. Luke, E. S. Lamb, M. R. E. Lamont, C. Joshi, Y. Okawachi, F. W. Wise, M. Lipson, U. Keller, and A. L. Gaeta, "Octave-spanning coherent supercontinuum generation in a silicon nitride waveguide," Opt. Lett. **40**, 5117–5120 (2015).
61. A. S. Mayer, A. Klenner, A. R. Johnson, K. Luke, M. R. E. Lamont, Y. Okawachi, M. Lipson, A. L. Gaeta, and U. Keller, "Frequency comb offset detection using supercontinuum generation in silicon nitride waveguides," Opt. Express **23**, 15440–15451 (2015).
62. T. Wang, D. K. T. Ng, S.-K. Ng, Y.-T. Toh, A. K. L. Chee, G. F. R. Chen, Q. Wang, and D. T. H. Tan, "Supercontinuum generation in bandgap engineered, back-end CMOS compatible silicon rich nitride waveguides: supercontinuum generation in bandgap engineered, back-end CMOS," Laser Photon. Rev. **9**, 498–506 (2015).
63. H. Zhao, B. Kuyken, S. Clemmen, F. Leo, A. Subramanian, A. Dhakal, P. Helin, S. Severi, E. Brainis, G. Roelkens, and R. Baets, "Visible-to-near-infrared octave spanning supercontinuum generation in a silicon nitride waveguide," Opt. Lett. **40**, 2177–2180 (2015).
64. A. Klenner, A. S. Mayer, A. R. Johnson, K. Luke, M. R. E. Lamont, Y. Okawachi, M. Lipson, A. L. Gaeta, and U. Keller, "Gigahertz frequency comb offset stabilization based on supercontinuum generation in silicon nitride waveguides," Opt. Express **24**, 11043–11053 (2016).
65. C. Herkommer, A. Billat, H. Guo, D. Grassani, C. Zhang, M. H. P. Pfeiffer, C.-S. Bres, and T. J. Kippenberg, "Mid-infrared frequency comb generation with silicon nitride nano-photonic waveguides," Nat. Photonics **12**, 330–335 (2018).
66. Y. Okawachi, M. Yu, J. Cardenas, X. Ji, A. Klenner, M. Lipson, and A. L. Gaeta, "Carrier envelope offset detection via simultaneous supercontinuum and second-harmonic generation in a silicon nitride waveguide," Opt. Lett. **43**, 4627–4630 (2018).
67. C. Lafforgue, S. Guerber, J. M. Ramirez, G. Marcaud, C. Alonso-Ramos, X. Le Roux, D. Marris-Morini, E. Cassan, C. Baudot, and F. Boeuf, "Broadband supercontinuum generation in nitrogen-rich silicon nitride waveguides using a 300 mm industrial platform," Photon. Res. **8**, 352–358 (2020).
68. J. P. Epping, T. Hellwig, M. Hoekman, R. Mateman, A. Leinse, R. G. Heideman, A. van Rees, P. J. van der Slot, C. J. Lee, and C. Fallnich, "On-chip visible-to-infrared supercontinuum generation with more than 495 THz spectral bandwidth," Opt. Express **23**, 19596–19604 (2015).
69. M. A. G. Porcel, F. Schepers, J. P. Epping, T. Hellwig, M. Hoekman, R. G. Heideman, P. J. M. van der Slot, C. J. Lee, R. Schmidt, R. Bratschitsch, C. Fallnich, and K.-J. Boller, "Two-octave spanning supercontinuum generation in stoichiometric silicon nitride waveguides pumped at telecom wavelengths," Opt. Express **25**, 1542–1554 (2017).
70. D. Grassani, E. Tagkoudi, H. Guo, C. Herkommer, F. Yang, T. J. Kippenberg, and C.-S. Brès, "Mid infrared gas spectroscopy using efficient fiber laser driven photonic chip-based supercontinuum," Nat. Commun. **10**, 1553 (2019).
71. H. Guo, W. Weng, J. Liu, F. Yang, W. Hänsel, C. S. Brès, L. Thévenaz, R. Holzwarth, and T. J. Kippenberg, "Nanophotonic supercontinuum-based mid-infrared dual-comb spectroscopy," Optica **7**, 1181–1188 (2020).
72. E. Tagkoudi, C. G. Amiot, G. Genty, and C.-S. Brès, "Extreme polarization-dependent supercontinuum generation in an uncladded silicon nitride waveguide," Opt. Express **29**, 21348–21357 (2021).
73. P. Manurkar, E. F. Perez, D. D. Hickstein, D. R. Carlson, J. Chiles, D. A. Westly, E. Baumann, S. A. Diddams, N. R. Newbury, K. Srinivasan, S. B. Papp, and I. Coddington, "Fully self-referenced frequency comb consuming 5 watts of electrical power," OSA Contin. **1**, 274–282 (2018).
74. K. Van Gasse, S. Uvin, V. Moskalenko, S. Latkowski, G. Roelkens, E. Bente, and B. Kuyken, "Recent advances in the photonic integration of mode-locked laser diodes," IEEE Photon. Technol. Lett. **31**, 1870–1873 (2019).